GF5025: Sistemas de observación de la atmósfera

Lidars y Nefobasímetros. Parte 1: Descripción general y aplicaciones

- Principios del Lidar
- Tipos de Lidar
- Nefobasímetro
- Aplicaciones
- Aplicaciones de Lidars y Nefos en Chile

Ricardo Muñoz M., 6/10/2021

Working Principle:

Physical picture in LIDAR remote sensing:

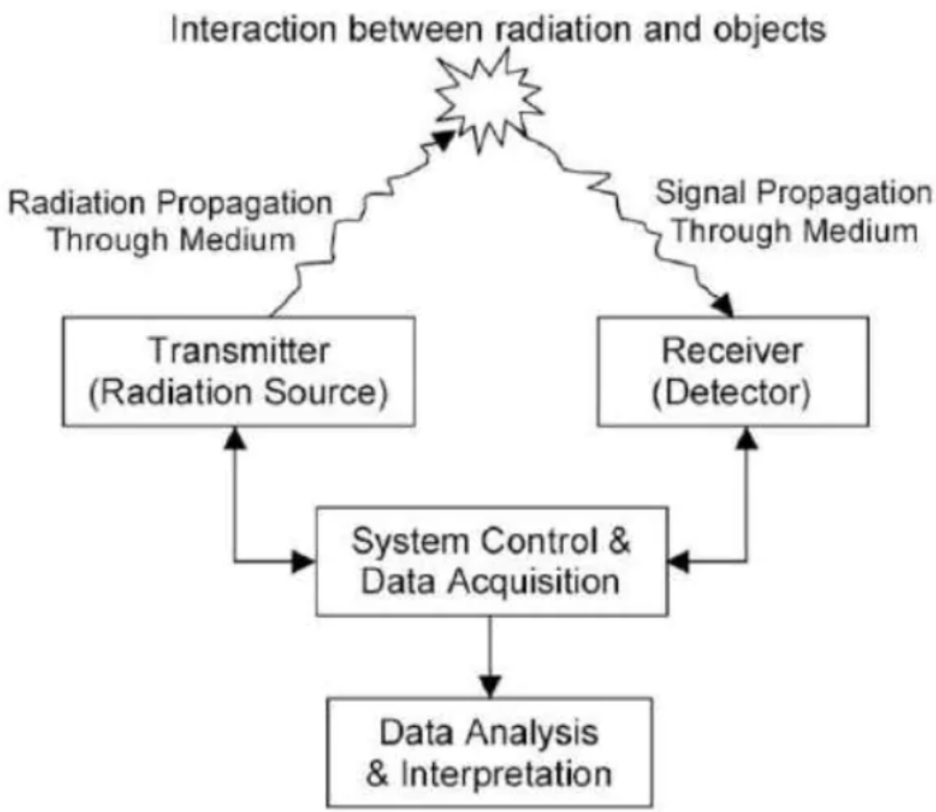

Presented by-
Rahul Sarnagat
M.Tech

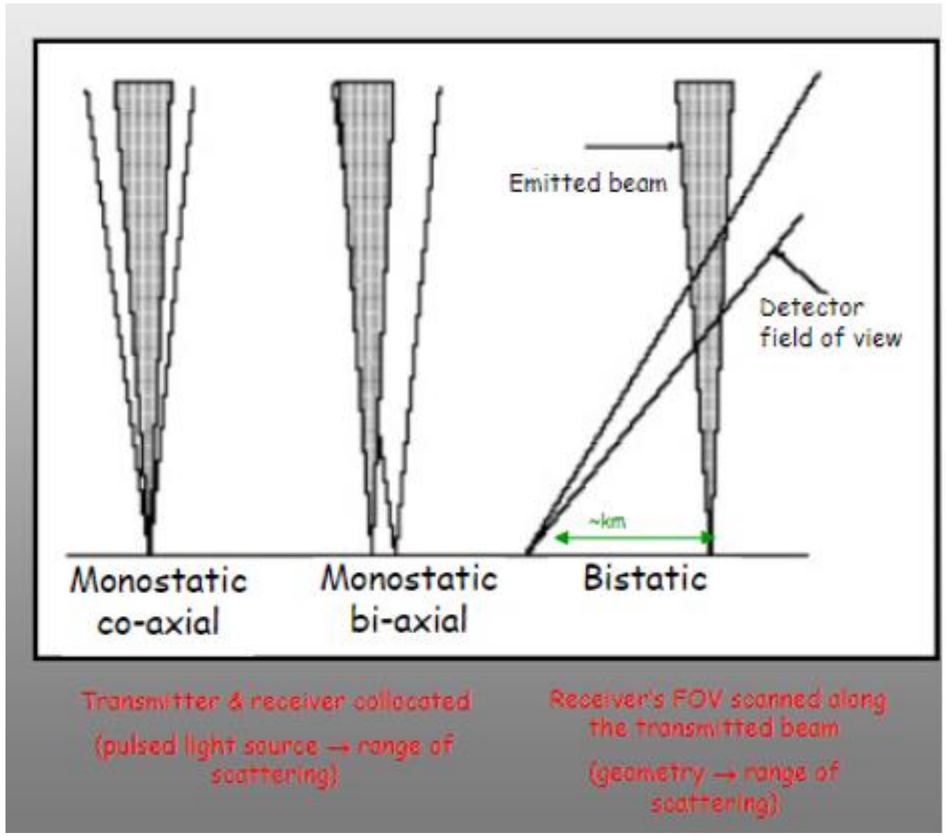

Philippe Keckhut et Andrea Pazmiño

LATMOS, Institut Pierre Simon Laplace, CNRS-UPMC-UVSQ, Paris, France

Present

- Networks of ground-based lidar systems as NDSC, EARLINET, etc
- Lidars on aircraft
- Space-based lidar (ALISSA, LITE, … CALIPSO program)

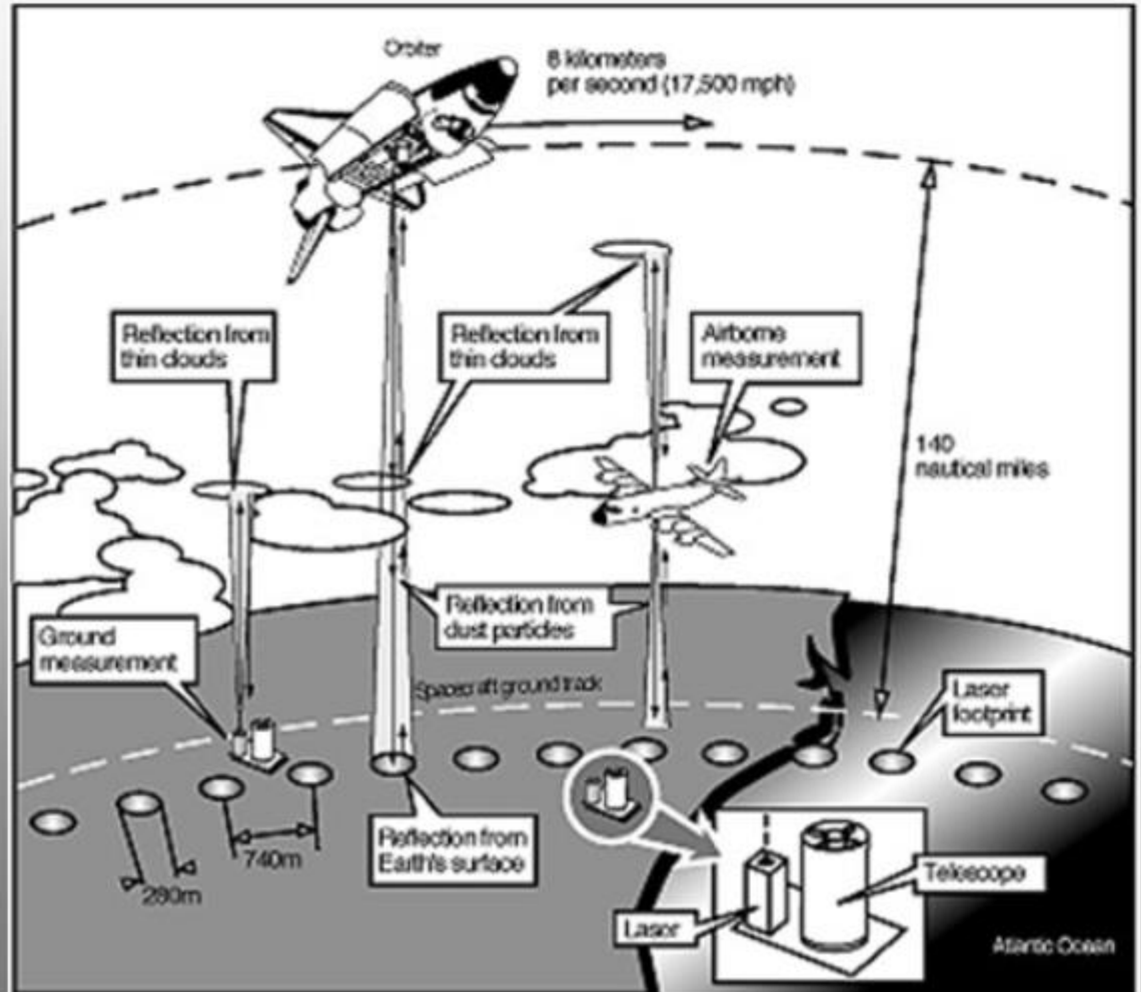

Philippe Keckhut et Andrea Pazmiño

LATMOS, Institut Pierre Simon Laplace, CNRS-UPMC-UVSQ, Paris, France

LIDAR: LIght Detection And Ranging

- **Active** remote sensing technique for measuring atmospheric parameters (**T**, ρ, **wind** and different **constituents**: H_2O, O_3, ..., **clouds**, **aerosols**)

  Same principle as radar but **0.1 < λ < 10 µm**

- **Principle**: emission of a light beam that interacts with the medium & detection of radiation backscattered towards the instrument

- Interactions with the Atmosphere:

- elastic (**Rayleigh**, **Mie**, **Resonance** scattering)
  inelastic (**Raman** scattering, **Fluorescence**)
  Absorption

Philippe Keckhut et Andrea Pazmiño

LATMOS, Institut Pierre Simon Laplace, CNRS-UPMC-UVSQ, Paris, France

Some Optical Interactions of Relevance to Laser Environmental Sensing

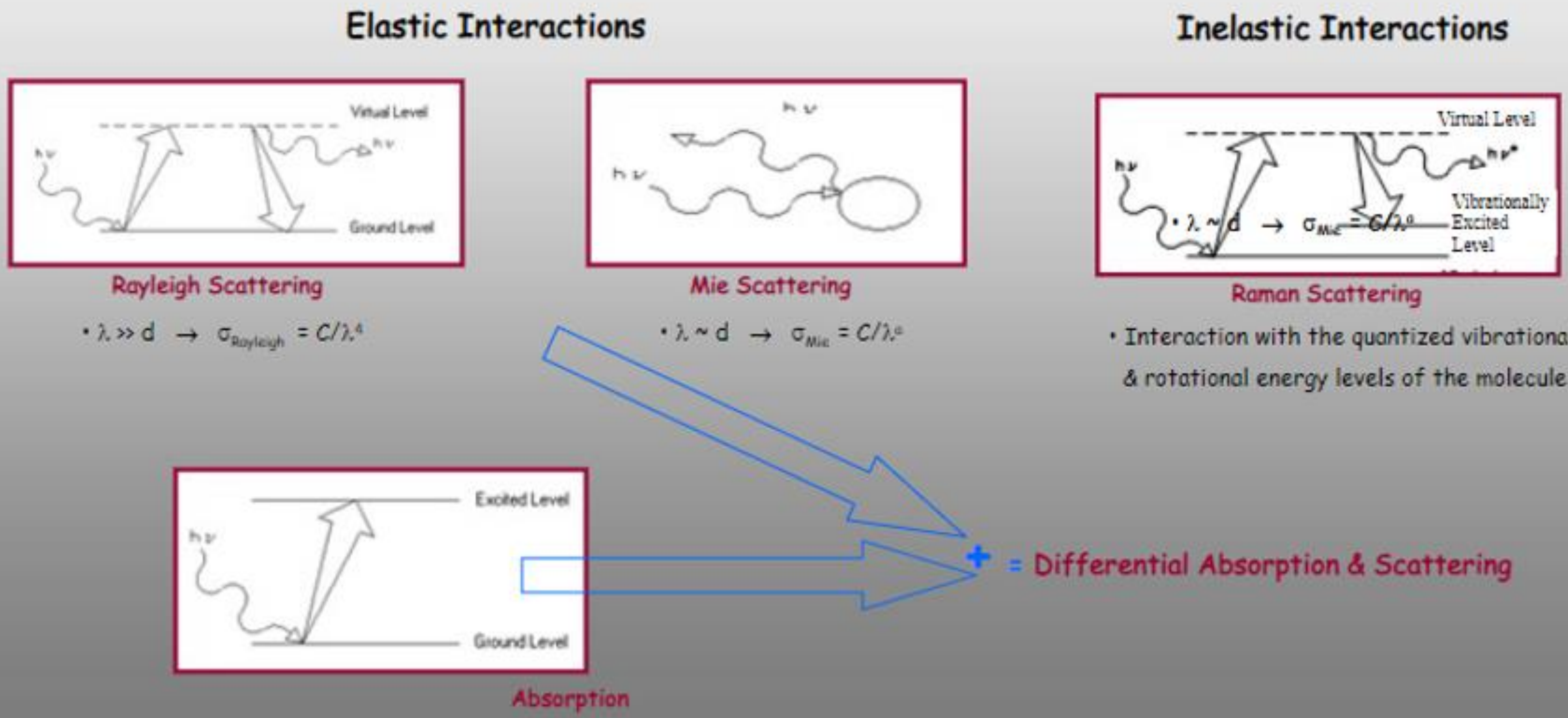

Philippe Keckhut et Andrea Pazmiño
LATMOS, Institut Pierre Simon Laplace, CNRS-UPMC-UVSQ, Paris, France

Block diagram of a generic lidar system

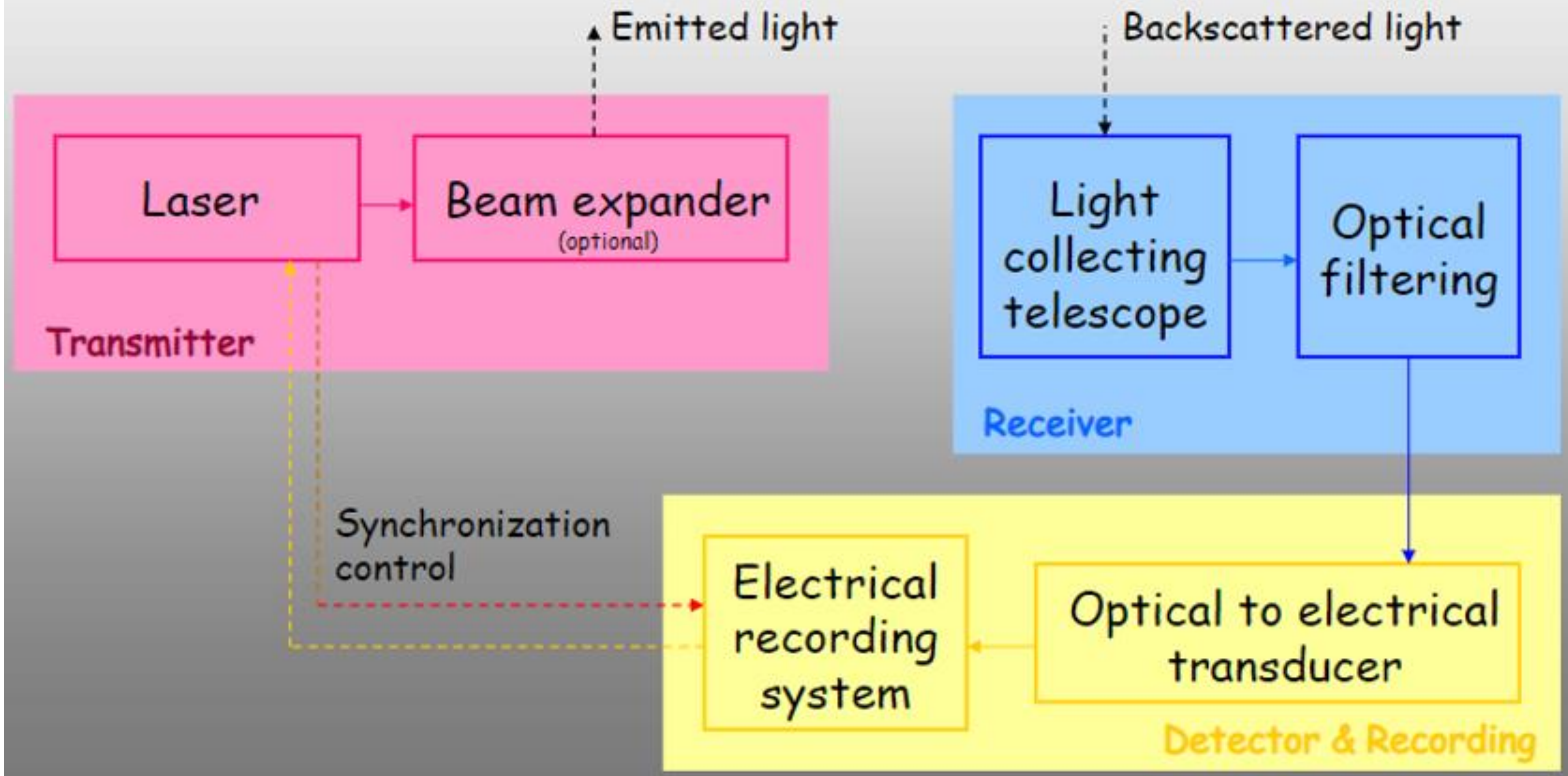

Philippe Keckhut et Andrea Pazmiño
LATMOS, Institut Pierre Simon Laplace, CNRS-UPMC-UVSQ, Paris, France

Ranging of pulsed monostatic lidar

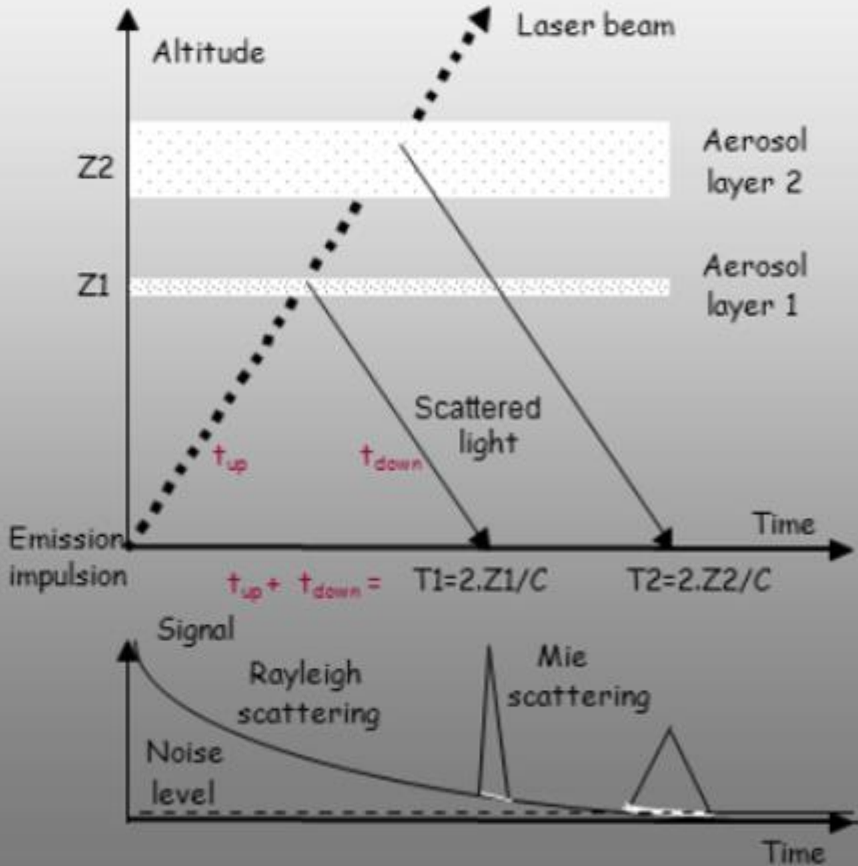

Each light pulse fired

⇓

Complete altitude scattering profile

$z = ct/2 \Rightarrow 1\ \mu s \equiv 150\ m$

Philippe Keckhut et Andrea Pazmiño

LATMOS, Institut Pierre Simon Laplace, CNRS-UPMC-UVSQ, Paris, France

Tipos de Lidar

Types of LIDAR:

- ELASTIC LIDAR

  Elastic backscatter LIDAR

  - Mie scattering

  -Rayleigh scattering

- INELASTIC LIDAR

  -Raman LIDAR

  -Differential absorption LIDAR(DIAL)

  -Doppler LIDAR

Presented by-
Rahul Sarnagat
M.Tech

Raman Lidar

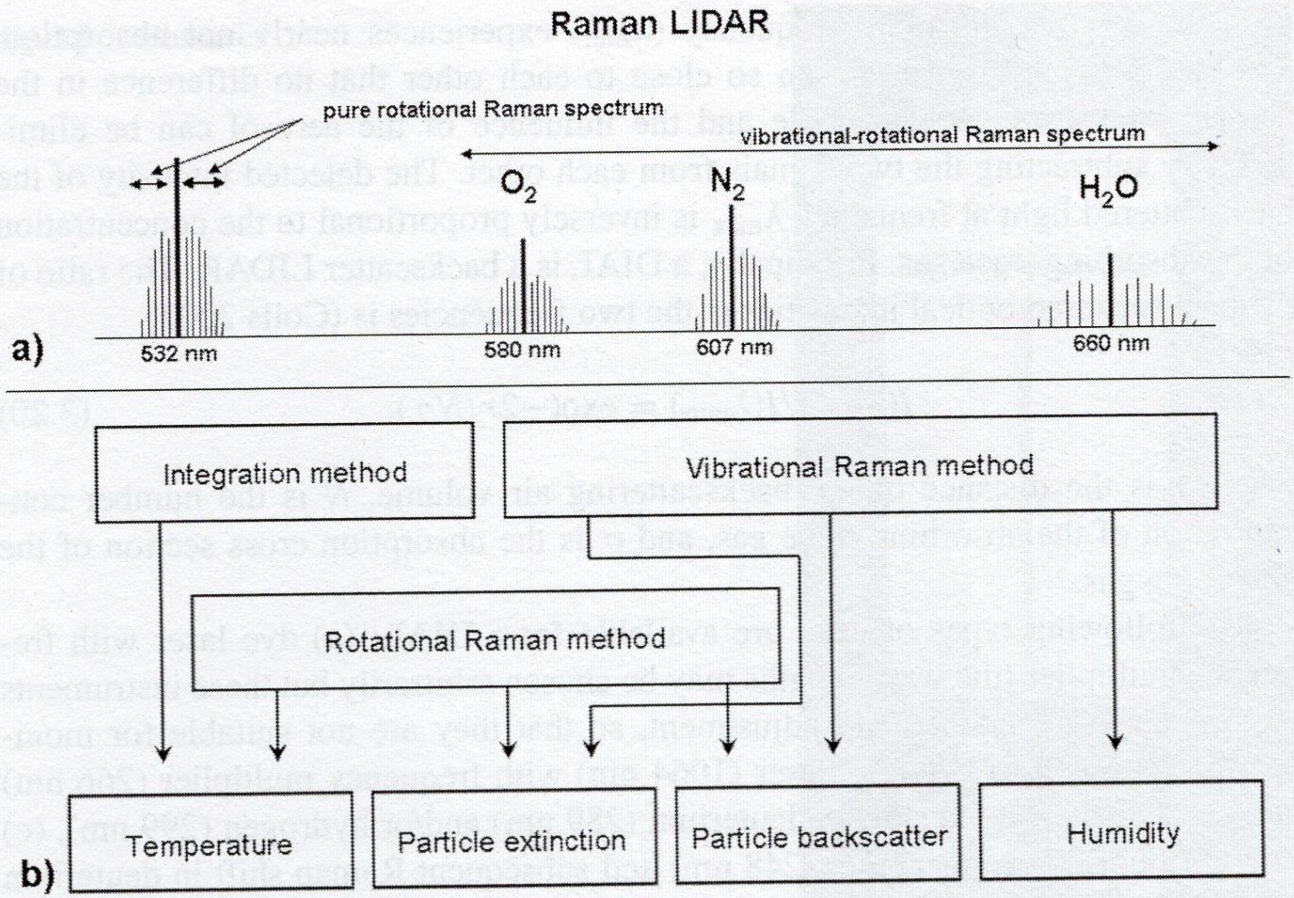

Fig. 3.10 (**a**) Schematic of the arrangement of Raman-shifted backscattered wavelengths, and (**b**) evaluation methods for a Raman-LIDAR

Differential absorption Lidar (DIAL):

mide perfiles de concentración de especies: H_2O, Ozono...

Se eligen 2 longitudes cercanas: una en banda de absorción de la especie y otra sin absorción. Efecto de aerosoles se supone idéntico, por lo que la razón entre intensidades recibidas en ambas bandas se relaciona con la concentración de la especie de interés.

Doppler Lidar

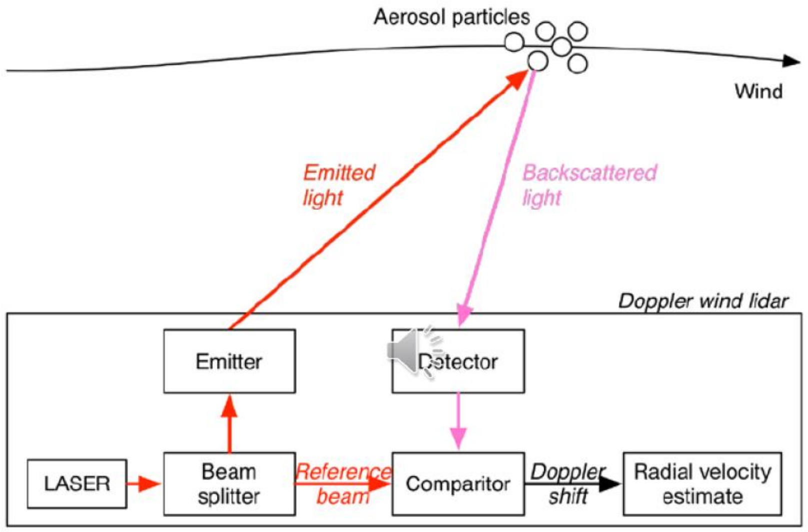

The WINDCUBE®v2 lidar remote sensor provides 200m vertical wind profiles on various possible locations, mapping wind speed and direction, turbulence, and wind shear. Leosphere - Vaisala

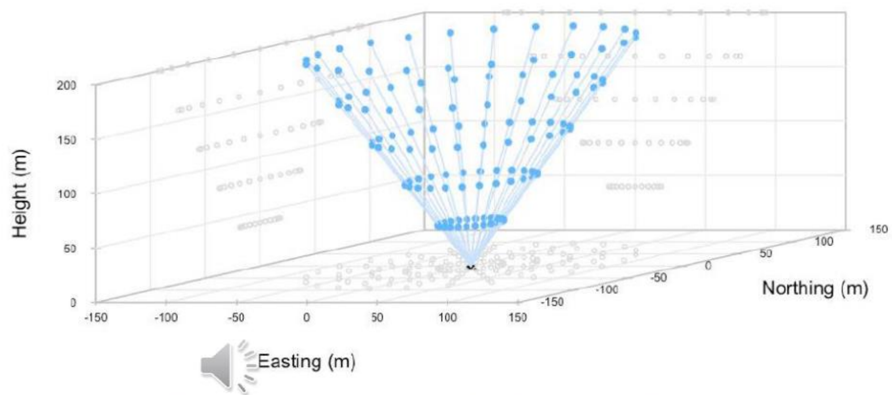

Figure 4. Visualization of measurement points in a conical scan

The lidar is shown by the black triangle. The round blue points indicate the nominal measurement locations associated with the probe and are shown projected onto the axes as grey points. In this case the angle from vertical is 25°, and the measurements are made every 15° around the azimuth. Measurements are spaced 40 m apart vertically.

Prof. P. Taylor slices: http://www.yorku.ca/pat/ESSE4230/

Nefobasímetro (nefo) o ceilómetro (cielómetro)


VAISALA

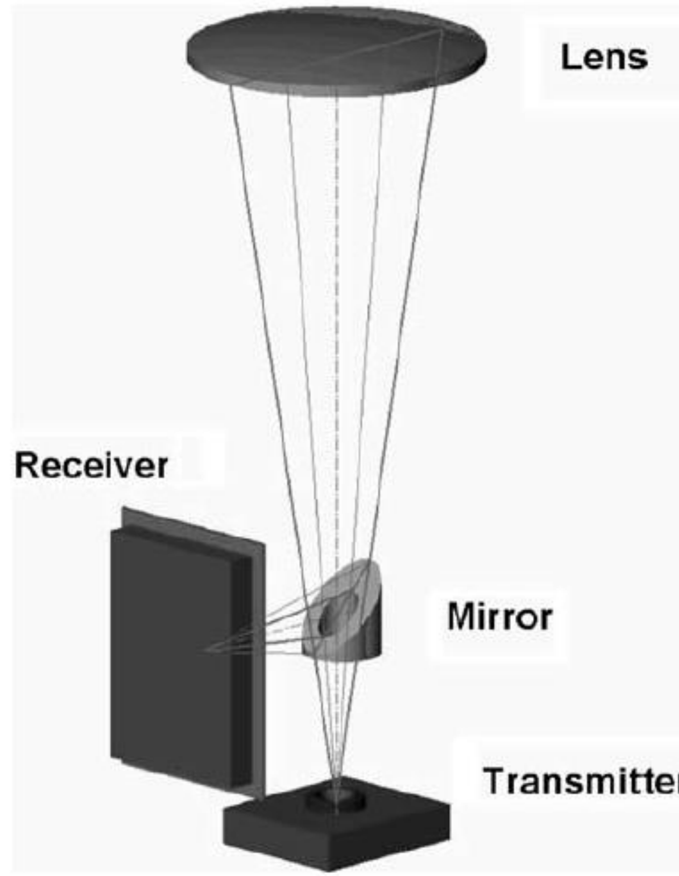
Lens
Receiver
Mirror
Transmitter

Table 1 Technical properties of the ceilometers CT25K and CL31

	CT25K	CL31
Measurement range (m)	0 – 7500	0 – 7500
Resolution (m)	15	10
Laser system	InGaAs MOCVD laser diode	InGaAs MOCVD laser diode
Wavelength (nm)	905	905
Pulse properties	100 ns, 1.6 μJ/pulse	110 ns, 1.2 μJ/pulse
Mean pulse repetition rate (Hz)	4369	8192

8192 Hz ===> 1 Pulso cada 122.070 ns

c = 3 x 10^8 m/s

Luz recorre 2 x 7.5 km en 50.000 ns

Si se promedian 2 s de mediciones, se promedian 16.384 perfiles

Si la señal de retorno se muestrea a 15 MHz, la resolución es 10 m

2.1 Simplified lidar equation

The optical power received by a ceilometer from distance x is

$$P(x,\lambda) = \frac{c}{2x^2} \underbrace{P_0 A \eta O(x) \Delta t}_{\text{instrument specific}} \times \underbrace{\beta(x,\lambda)\tau^2(x,\lambda)}_{\text{attenuated backscatter}} , \qquad (1)$$

Aplicaciones de nefobasímetros

- altura de base de nubes
- altura de capa de mezcla
- concentración de aerosoles
- visualización dinámica
- intercomparaciones
- otras:
    - intensidad de precipitación
    - validación de modelos
    - información accesoria
    - ...

Advances in Space Research 63 (2019) 1708–1718

A comprehensive statistical study of cloud base height using ceilometer over western India

Rajesh Vaishnav [a], Som Sharma [a,*], K.K. Shukla [a,c], Prashant Kumar [b], S. Lal [a]

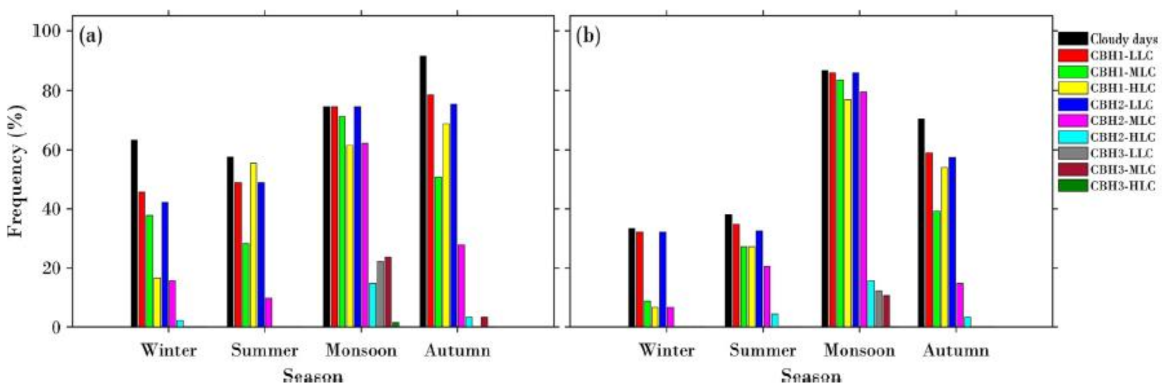

Fig. 5. Seasonal cloud occurrence frequency for LLC, MLC, and HLC from CBH1, CBH2 and CBH3 using ceilometer CL31 during the year (a) 2014 and (b) 2015.

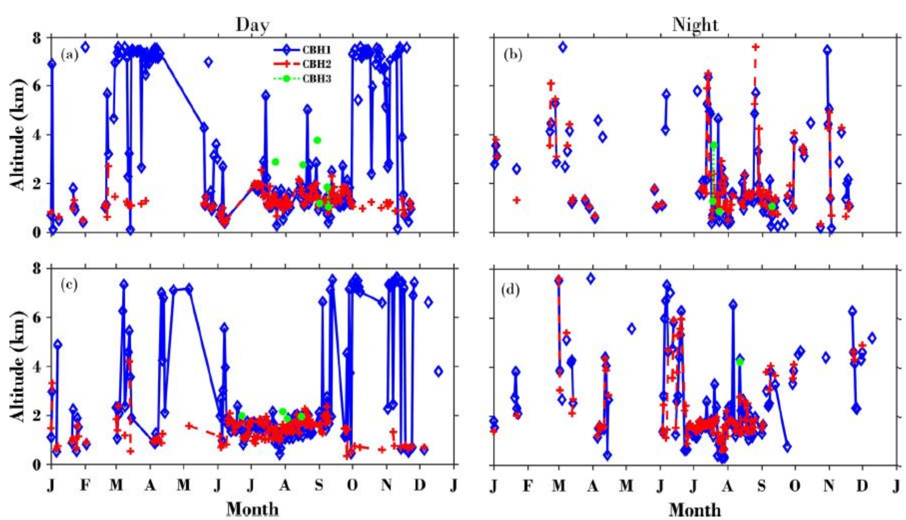

Fig. 9. Cloud characteristic during (a) daytime and (b) nighttime during 2014, and (c) daytime and (d) nighttime for 2015 using ceilometer data.

RESEARCH ARTICLE

Quarterly Journal of the Royal Meteorological Society

Atmospheric boundary-layer characteristics from ceilometer measurements. Part 1: A new method to track mixed layer height and classify clouds

Simone Kotthaus[1,2] | C. Sue B. Grimmond[1]

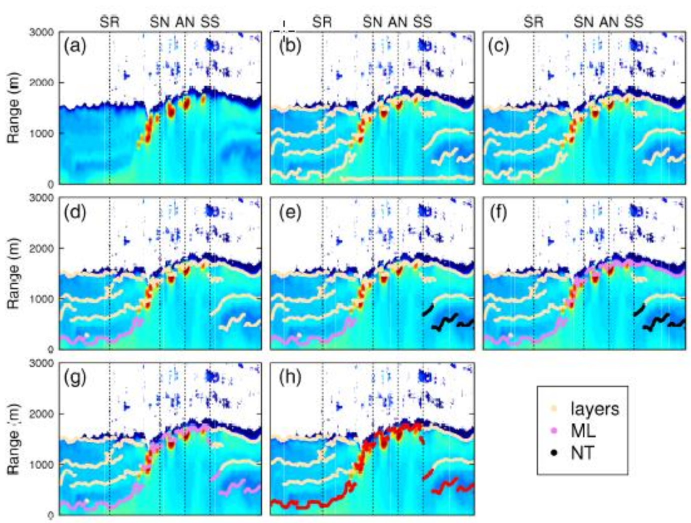

FIGURE 4 Illustration of selected CABAM steps: (a) logarithm of cleaned and smoothed attenuated backscatter from Vaisala CL31 in arbitrary units for 26 hr detection period (section 3.1.1), (b) as (a) with initial layers connecting points of significant vertical gradients (Figure 2), (c) as (b) after quality control removed physically unreasonable layer in near range (Suppl. S2.1 in File S1), (d) before sunrise (Figure S1, File S1): mixed-layer (ML) detected as lowest layer around sunrise and traced back to midnight, (e) after sunset (Figure S2, File S1): nocturnal layer (NT) detected as lowest layer before midnight and traced back to sunset, (f) morning transition (Figure S3, File S1): ML connected to other layers before solar noon, (g) evening transition (Figure S5, File S1): ML connected to NT incorporating layers in-between, and (h) final layer result (ML + additional layers in residual layer) after excluding layers of short duration or low density. SR = sunrise; SN = solar noon; AN = afternoon; and SS = sunset [Colour figure can be viewed at wileyonlinelibrary.com]

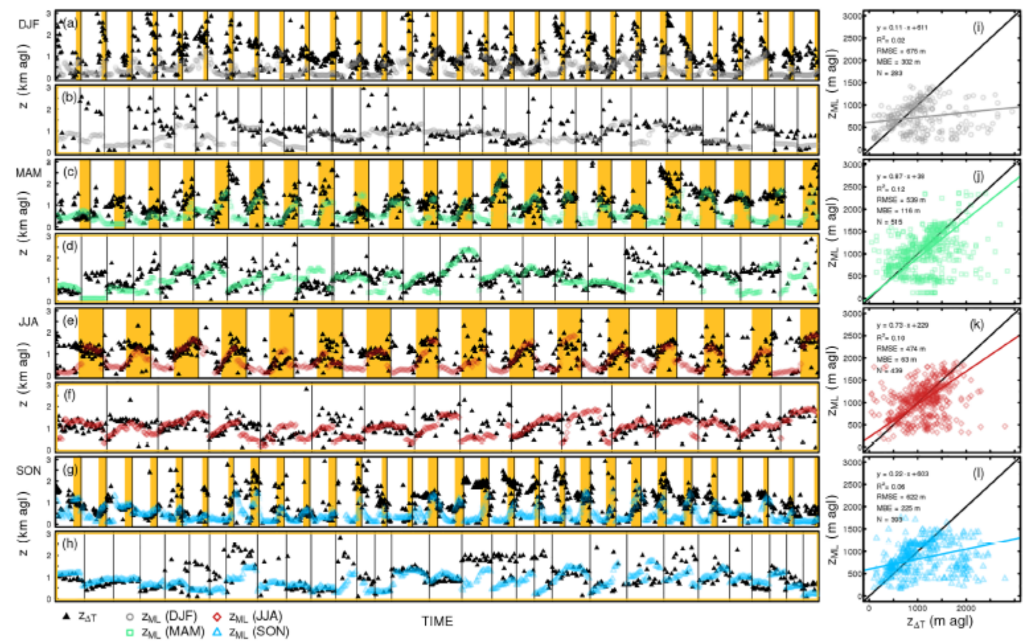

FIGURE 5 Mixed layer height Z_{ML} detected from ALC observations (section 3.2.1) for day_{SR} periods with cloud-free conditions (section 3.2.2) and at least four values (1 hr) of temperature inversion height $z_{\Delta T}$ estimates from AMDAR profile observations (section 3.1.3) >4 hr after sunrise: (a, c, e, g) full day_{SR} periods in time relative to sunrise are shown by season, (b, d, f, h) subset of times >4 hr after sunrise with no cloud detected below 3,000 m (marked by shading in a, c, e, g), (i–l) direct comparison of $z_{\Delta T}$ and z_{ML} for respective subsets with linear regression statistics. N is the number of sample pairs. Vertical lines in (a–h) denote change between day_{SR} periods [Colour figure can be viewed at wileyonlinelibrary.com]

Boundary-Layer Meteorol (2007) 124:117–128
DOI 10.1007/s10546-006-9103-3

Retrieval of mixing height and dust concentration with lidar ceilometer

**Christoph Münkel · Noora Eresmaa ·
Janne Räsänen · Ari Karppinen**

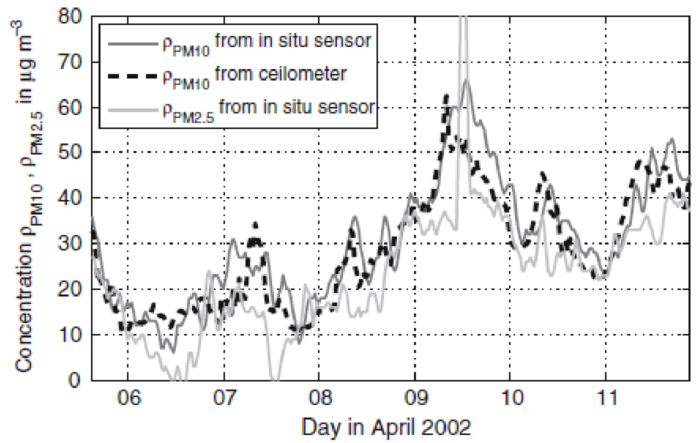

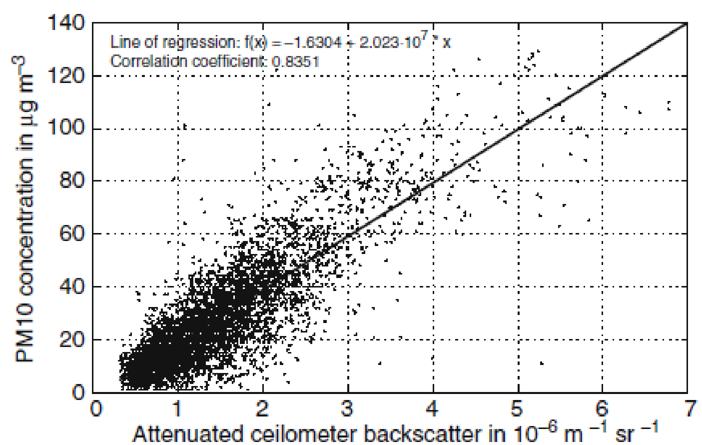

Atmos. Meas. Tech., 9, 4387–4398, 2016
www.atmos-meas-tech.net/9/4387/2016/
doi:10.5194/amt-9-4387-2016

Ceilometer evaluation of the eastern Mediterranean summer boundary layer height – first study of two Israeli sites

Leenes Uzan[1,2], Smadar Egert[1], and Pinhas Alpert[1]

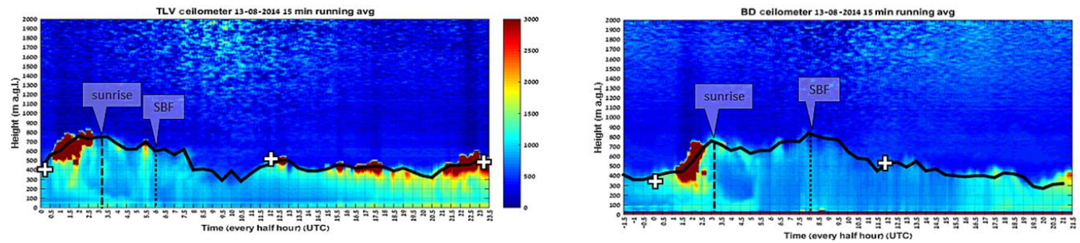

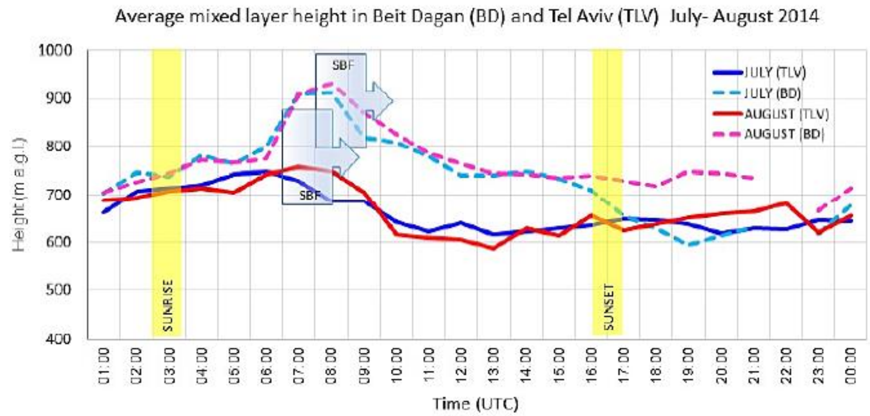

WRF-Chem vs. ceilometers for dust penetration on 02.03.14

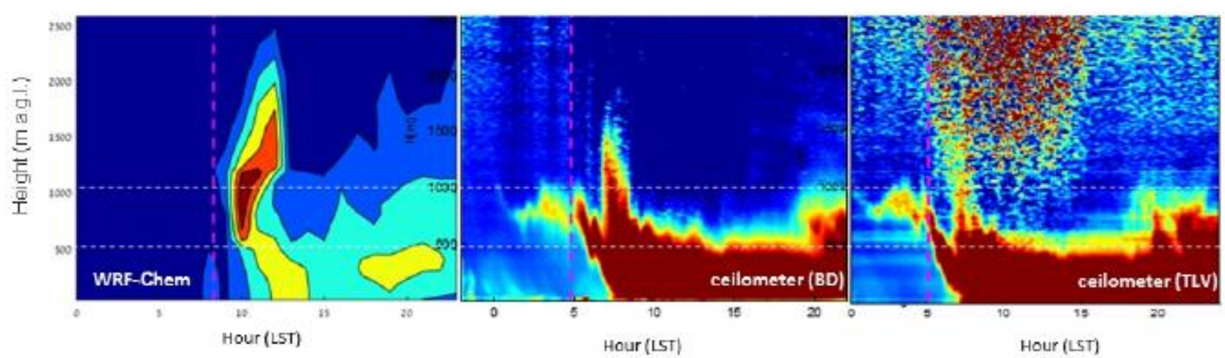

Atmospheric Environment 43 (2009) 5847–5852

Simultaneous observations of boundary-layer aerosol layers with *CL31* ceilometer and 1064/532 nm *lidar*

I.G. McKendry[a,*], D. van der Kamp[a], K.B. Strawbridge[b], A. Christen[a], B. Crawford[a]

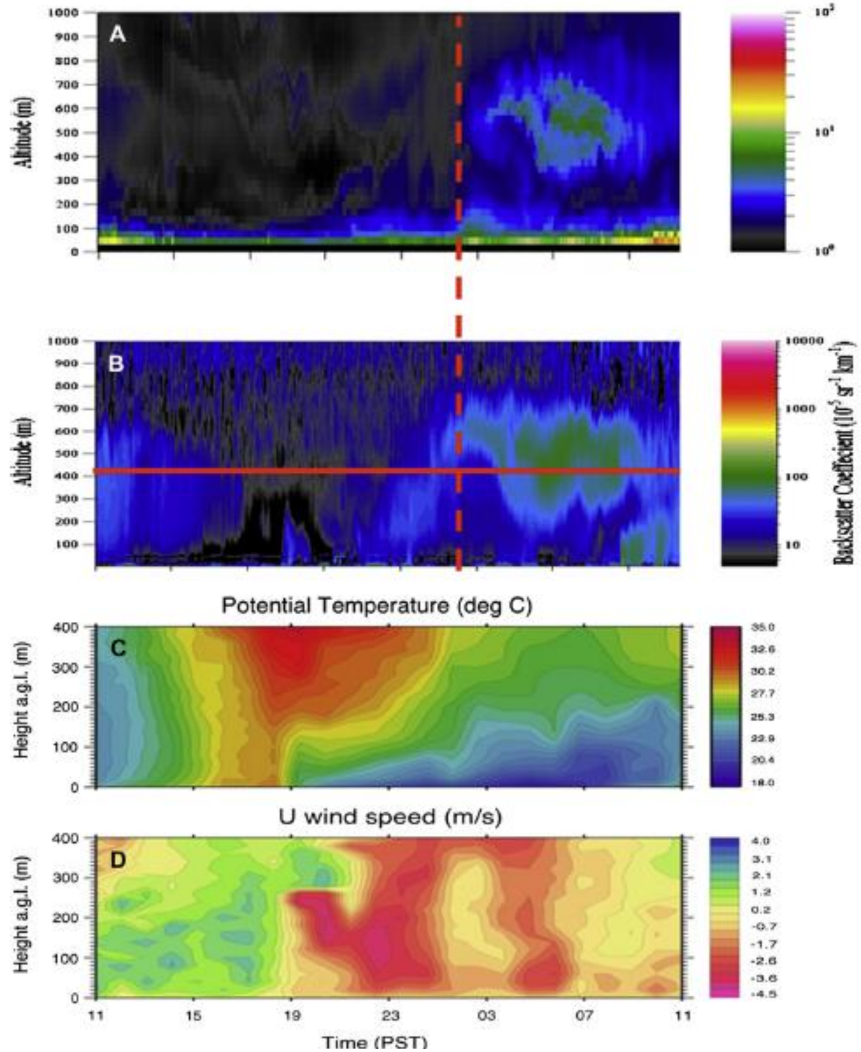

Fig. 3. Observations during 14–15 August 2008 showing elevated layer structure observed at (A) CORALNet-UBC (B) ceilometer (note red solid line denotes top of 400 m layer sampled by tethered balloon) and Cemetery tethered balloon observations of (C) potential temperature and (D) east-west wind component. See Fig. 1 for locations.

Ceilometer-Based Rain-Rate Estimation: A Case-Study Comparison With S-Band Radar and Disdrometer Retrievals in the Context of VORTEX-SE

Francesc Rocadenbosch, *Senior Member, IEEE*, Rubén Barragán, Stephen J. Frasier, *Senior Member, IEEE*, Joseph Waldinger, David D. Turner, Robin L. Tanamachi, and Daniel T. Dawson, II

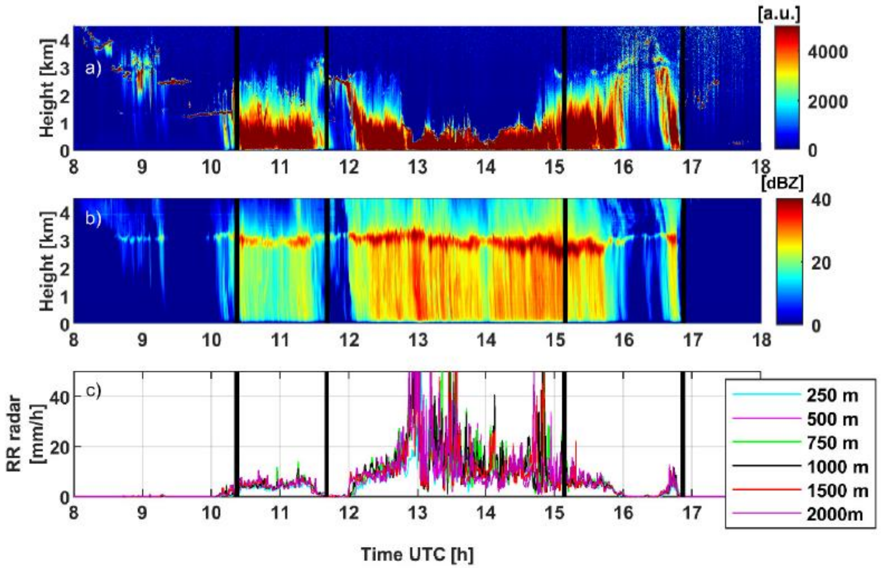

Fig. 7. Overview of March 31, 2016, rain episode. (a) Ceilometer range-corrected lidar signal [a.u.] versus time. (b) Radar reflectivity factor [dBZ] computed after (22). (c) RR [mm/h] time series measured by the radar at different heights, from 250 up to 2000 m. Vertical lines delimit the early-and late-morning time intervals discussed in Section V. Temporal resolution [(a)–(c)] is 16 s. Spatial (height) resolution [(a)–(c)] (see Table I).

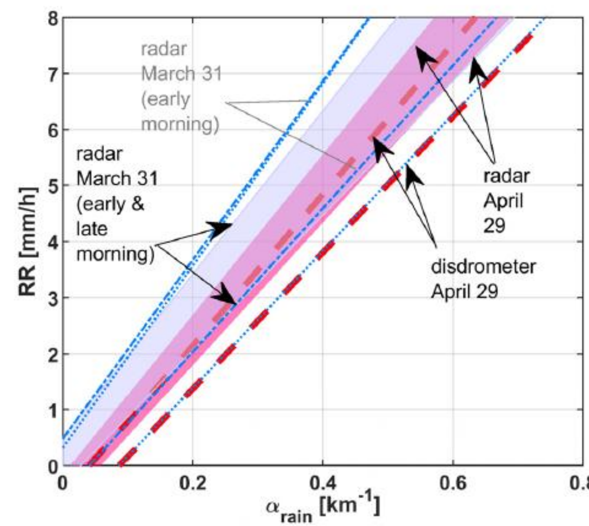

Fig. 10. Comparison between April 29 and March 31 RR–α models (see text).

Geosci. Model Dev., 14, 43–72, 2021
https://doi.org/10.5194/gmd-14-43-2021

Geoscientific Model Development
Open Access
EGU

Ground-based lidar processing and simulator framework for comparing models and observations (ALCF 1.0)

Peter Kuma[1], Adrian J. McDonald[1], Olaf Morgenstern[2], Richard Querel[3], Israel Silber[4], and Connor J. Flynn[5]

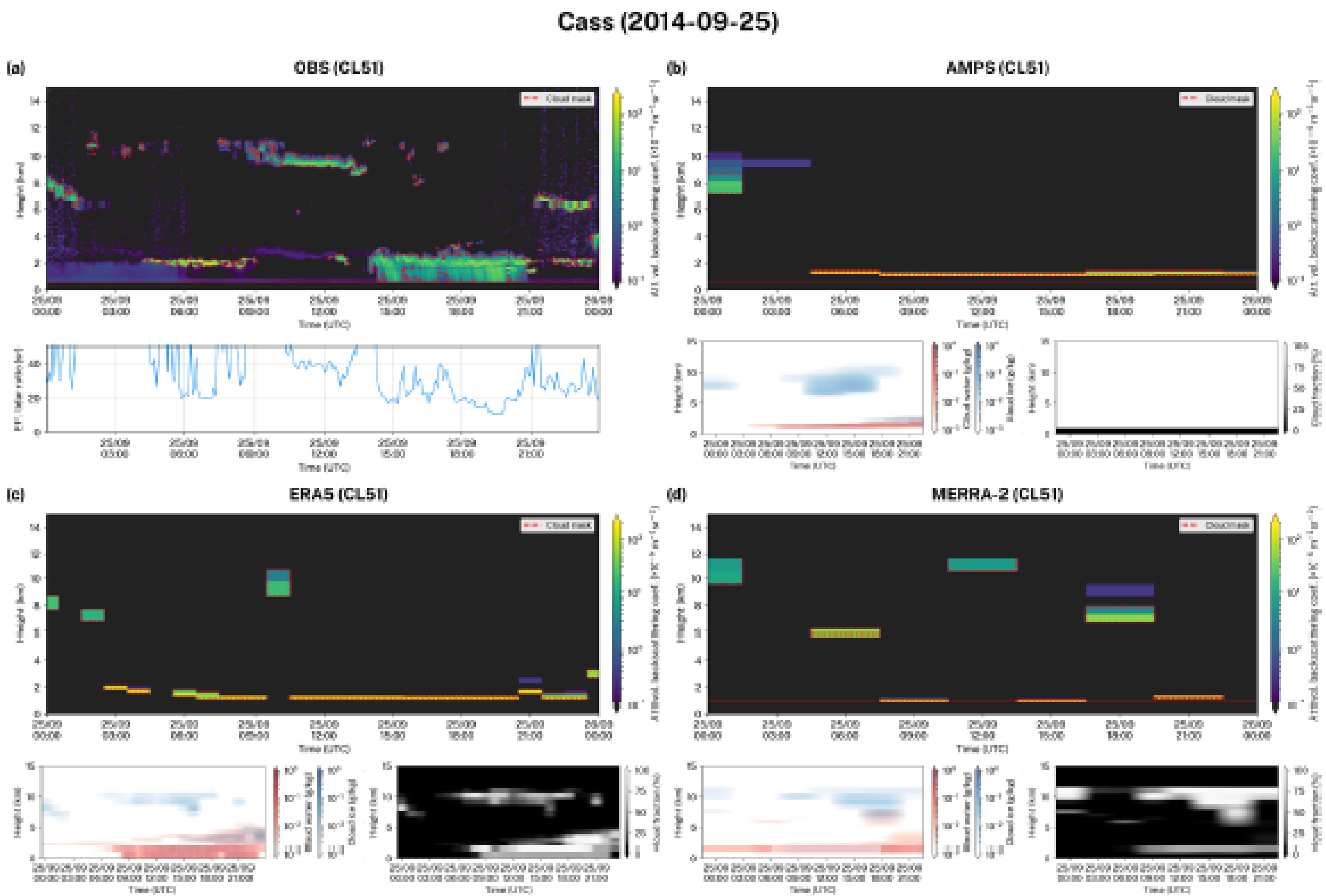

Atmos. Meas. Tech., 11, 593–609, 2018
https://doi.org/10.5194/amt-11-593-2018

Atmospheric Measurement Techniques
Open Access
EGU

All-sky photogrammetry techniques to georeference a cloud field

Pierre Crispel[1,a] and Gregory Roberts[1,2]

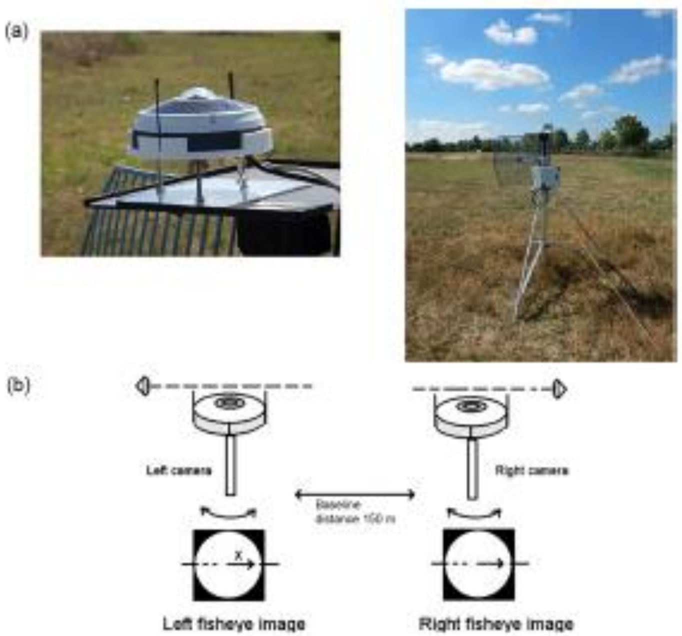

Figure 1. (a) VIVOTEK FE8391-V fisheye camera and installation structure. **(b)** Vertical sights on the camera housing allow visual inter-camera alignment in the horizontal plane.

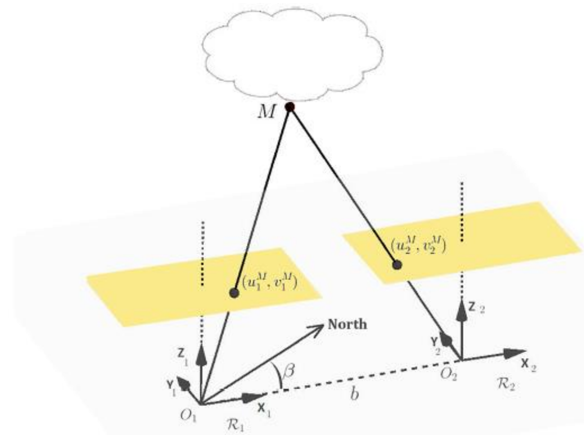

Figure 5. Ideal camera configuration. Camera coordinate systems are frontally aligned with optical axis $z_{1,2}$ oriented towards zenith. Optical centers $O_{1,2}$ are in the same altitude plane. The baseline distance is denoted b and North bearing of O_1O_2 axis is denoted β. In this ideal configuration, assuming that we have identical pinhole centered cameras, corresponding pixels $\left(u_1^M, v_1^M\right)$ and $\left(u_2^M, v_2^M\right)$ are row-aligned on the imagers $\left(\text{i.e., } v_1^M = v_2^M\right)$.

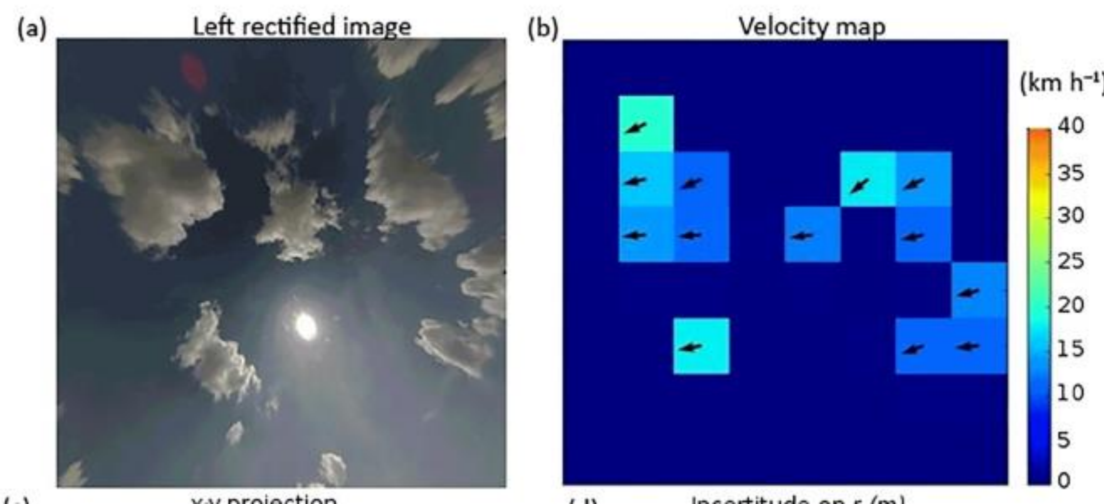

Aplicaciones de Lidars y Nefos en Chile

- DMC (aeronáutica)
  - nefos en todos los aeropuertos
- DMC-MMA (calidad del aire)
  - nefo en Santiago y Puchuncaví
  - Lidar en Santiago (2011)
- DGF:
  - nefo en Santiago (2007-2021)
  - nefo en Antofagasta (2013-2016)
  - nefo en Coyhaique (2018-2021)
- Meteodata Ltda.: nefos para calidad del aire en minería
- U. de Concepción: Centro CEFOP
- USACH: Lidar en Antártica
- Leipzig/UMAG: Lidar++ en Punta Arenas
- Doppler-Lidars en uso para energía eólica

Aerosol and Air Quality Research, 12: 8–19, 2012

ISSN: 1680-8584 print / 2071-1409 online
doi: 10.4209/aaqr.2011.08.0133

Variability of Urban Aerosols over Santiago, Chile: Comparison of Surface PM_{10} Concentrations and Remote Sensing with Ceilometer and Lidar

Ricardo C. Muñoz[1*], Ricardo I. Alcafuz[2]

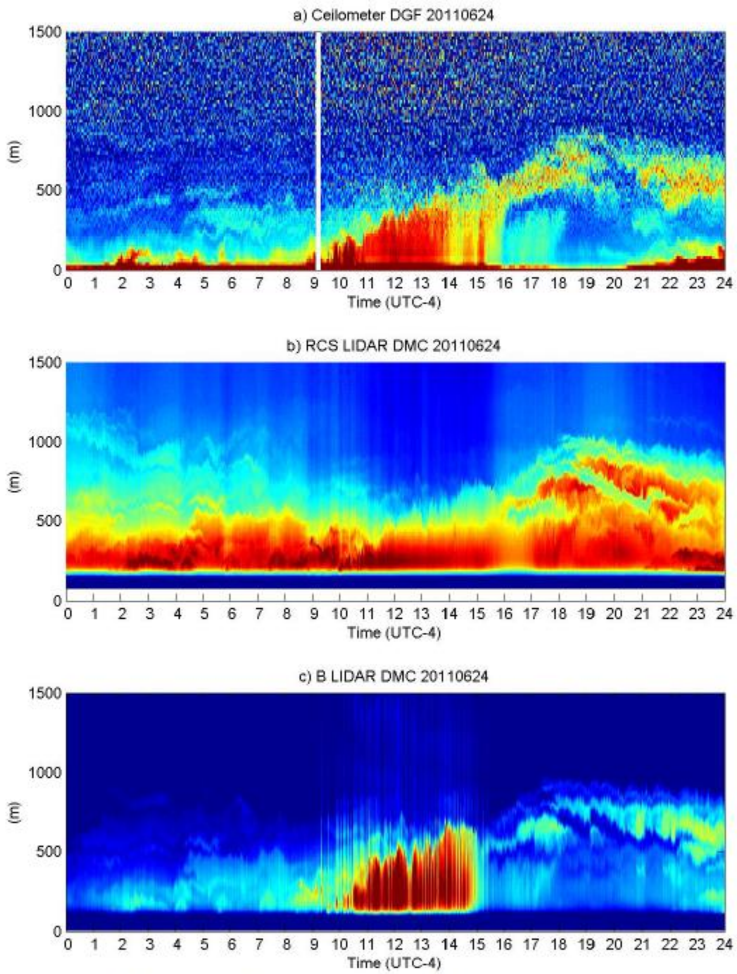

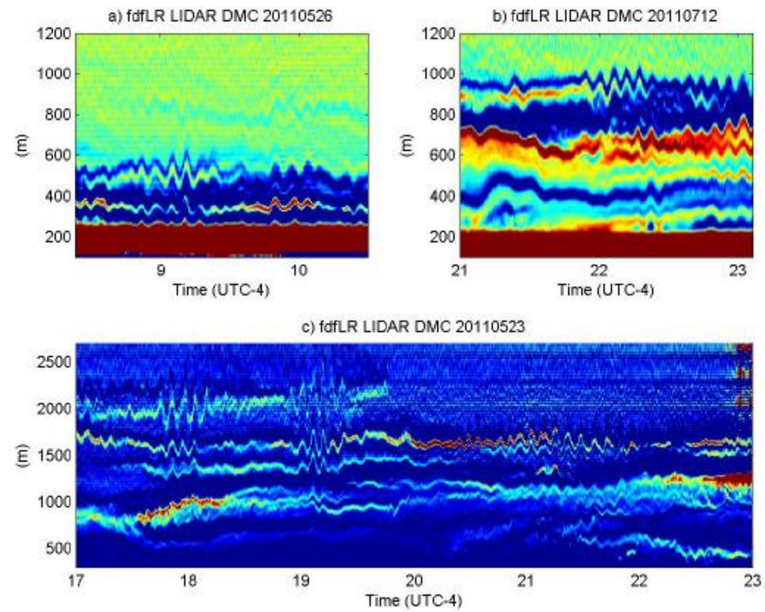

Fig. 8. Data for 24 June 2011. a) Ceilometer backscatter intensities, b) Lidar range corrected signal, c) Lidar aerosol backscatter.

Daytime Mixed Layer over the Santiago Basin: Description of Two Years of Observations with a Lidar Ceilometer

RICARDO C. MUÑOZ AND ANGELLA A. UNDURRAGA*

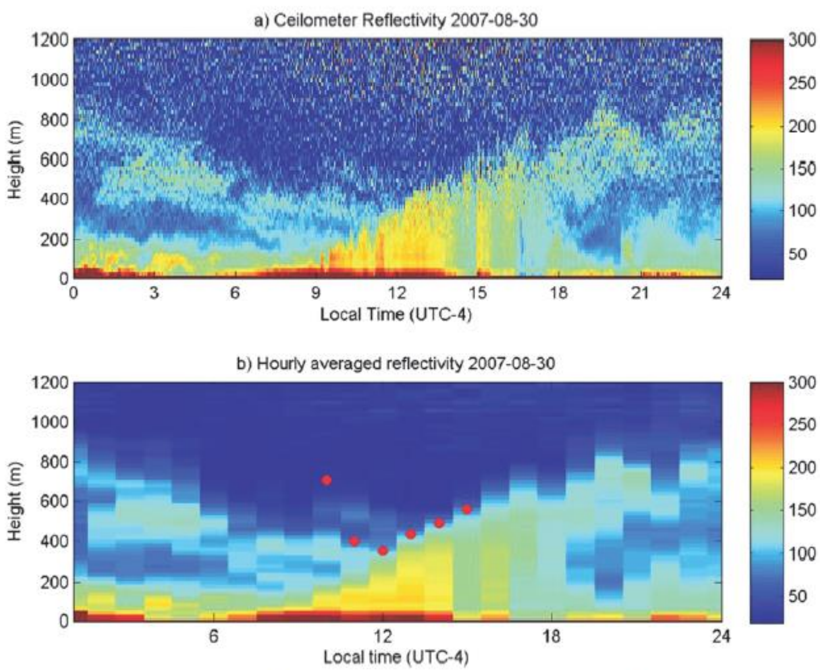

FIG. 2. (a) Instantaneous backscatter field measured by ceilometer CL31 for 30 Aug 2007. Temporal resolution is 4 s and vertical resolution is 20 m. Color scale is in backscatter units (see text). (b) As in (a), but for hourly averaged backscatter profiles. Red circles show MH retrieved by the algorithm described in the text. Retrievals at 1000 and 1100 LT were filtered out of the final analysis.

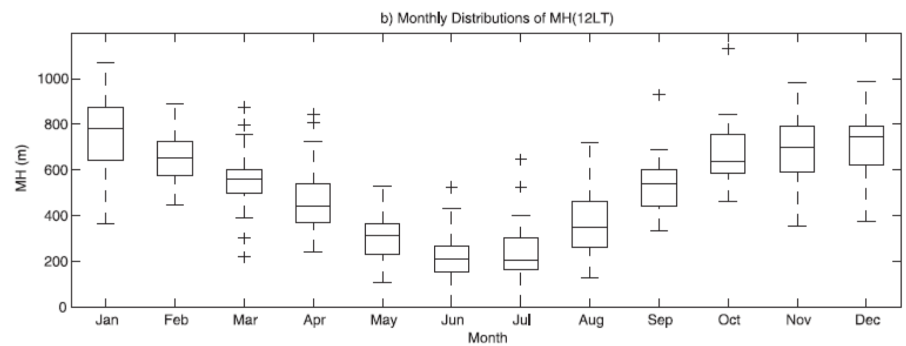

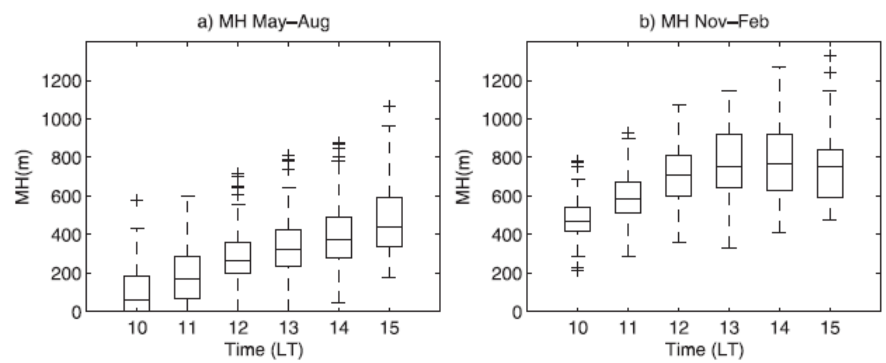

FIG. 7. (a) Boxplots of hourly distributions of MH for the period May–August (sunrise time ~0800 LT). (b) As in (a), but for November–February (sunrise time ~0600 LT).

Raco Wind at the Exit of the Maipo Canyon in Central Chile: Climatology, Special Observations, and Possible Mechanisms

RICARDO C. MUÑOZ,[a] LAURENCE ARMI,[b] JOSÉ A. RUTLLANT,[a,c] MARK FALVEY,[a,d]
C. DAVID WHITEMAN,[e] RENÉ GARREAUD,[a,f] ANDRÉS ARRIAGADA,[a,d] FEDERICO FLORES,[d]
AND NICOLÁS DONOSO[d,g]

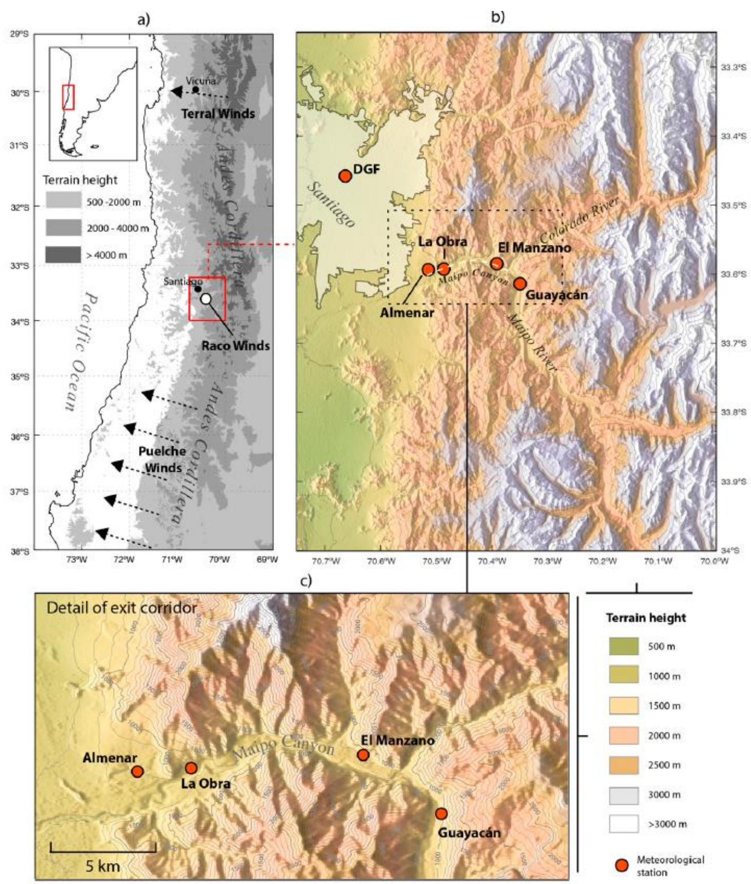

FIG. 1. (a) Topography of central Chile and its location in South America (inset). (b) Maipo River drainage network and easterly portion of Santiago Valley. Red circles mark sites with data used in the paper: Department of Geophysics (DGF) in downtown Santiago, Almenar (ALM), La Obra (LOB), El Manzano (MAN), and Guayacán (GUA). (c) Close-up of Maipo Canyon exit corridor.

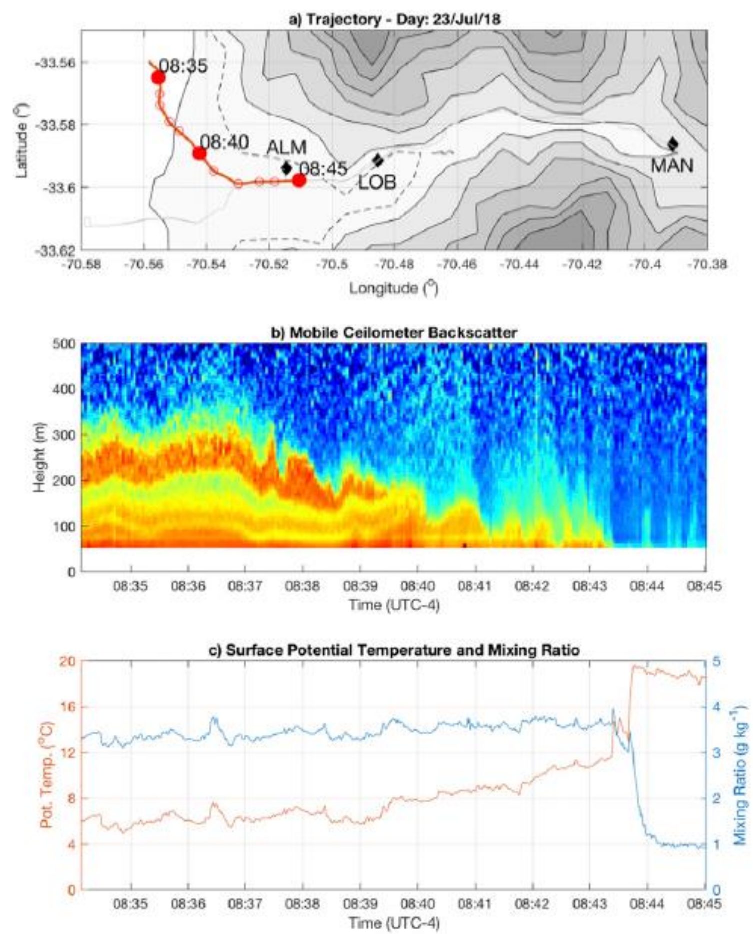

FIG. 17. As in Fig. 16, but for the mobile ceilometer transect in the period between 0834 and 0845 LT 23 Jul 2018.

Investigation of a Nocturnal Cold-Air Pool in a Semiclosed Basin Located in the Atacama Desert

FEDERICO FLORES,[a] ANDRÉS ARRIAGADA,[a] NICOLÁS DONOSO,[a,b,c] ANDRÉS MARTÍNEZ,[a] ALDO VISCARRA,[a]
MARK FALVEY,[a] AND RAINER SCHMITZ[a]

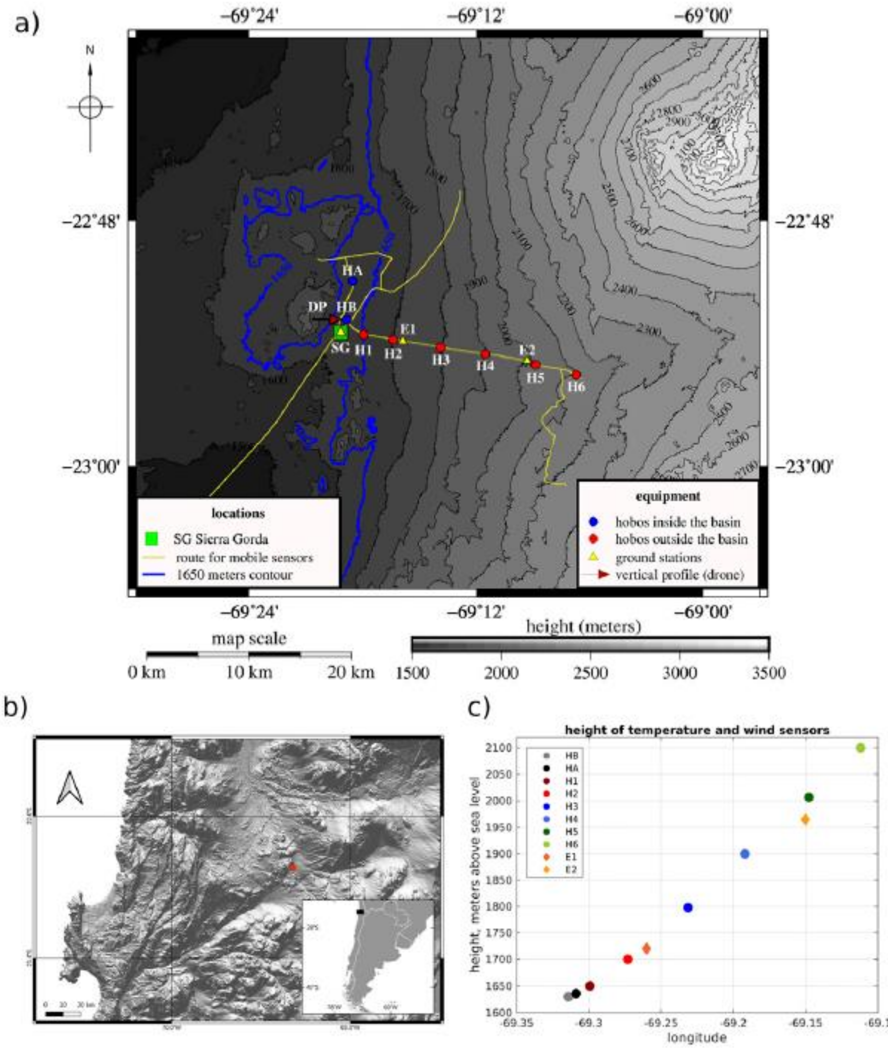

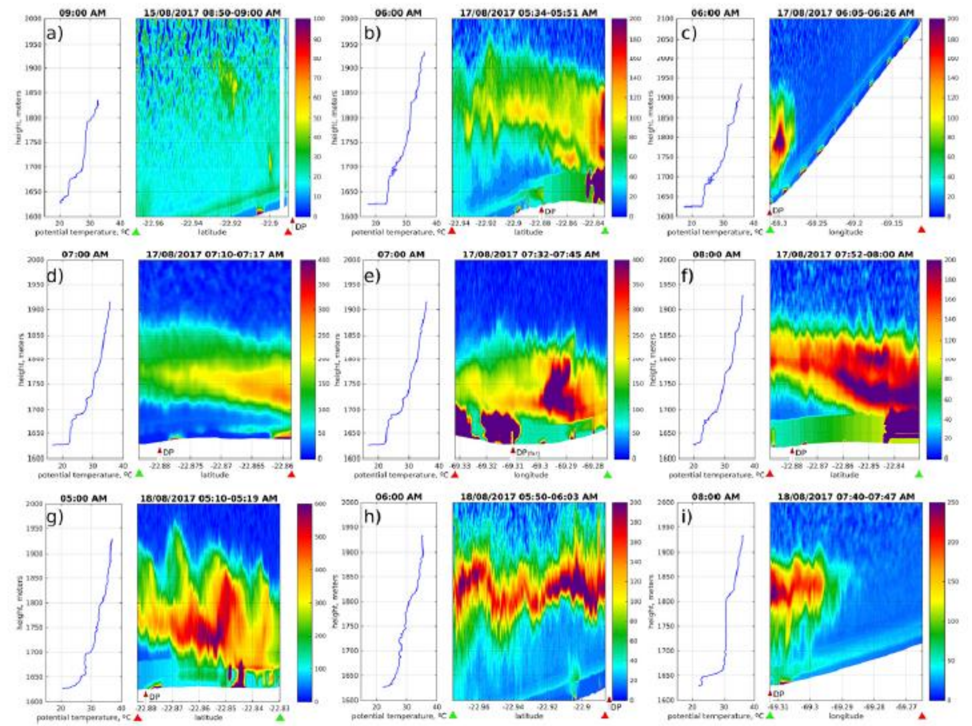

FIG. 14. Mobile ceilometer measurements and drone vertical profile of potential temperature. The ceilometer route for each case is included in Fig. 13. The green and red triangles indicate the start and the end of the route, respectively. The red arrow indicates the location of the drone profile. The color scale represents the laser ceilometer backscatter coefficient (arbitrary scale). In (e) there is a large separation between the drone profile location and the ceilometer measurement route.

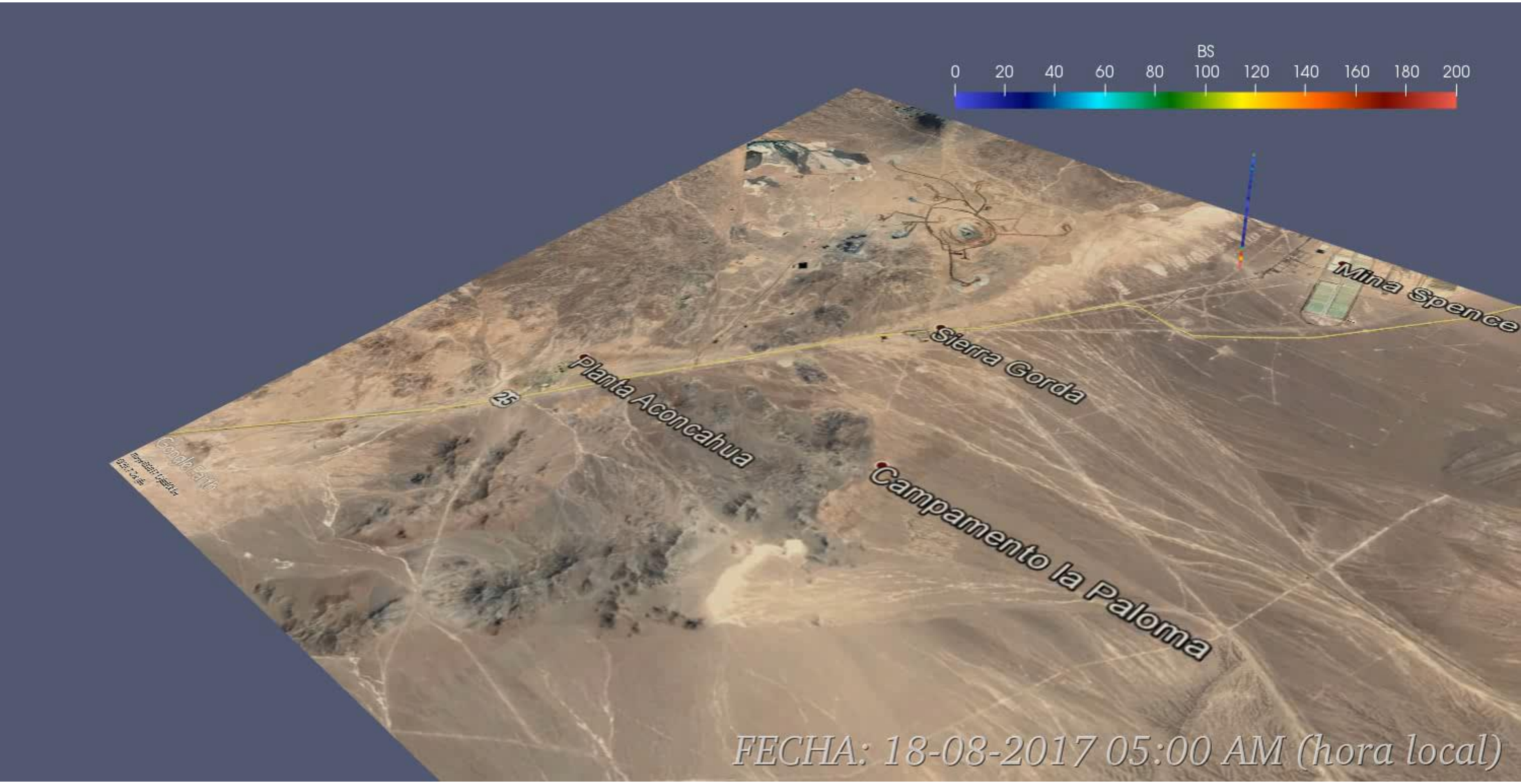

BS
0 20 40 60 80 100 120 140 160 180 200
Mina Spence
Sierra Gorda
Planta Aconcahua
25
Campamento la Paloma
FECHA: 18-08-2017 05:00 AM (hora local)

CARACTERIZACIÓN OBSERVACIONAL DE EVENTOS DE TERRAL EN EL VALLE DEL RÍO PELAMBRES

TESIS PARA OPTAR AL GRADO DE MAGÍSTER EN METEOROLOGÍA Y CLIMATOLOGÍA

ANDRÉS ELIESER ARRIAGADA PINTO

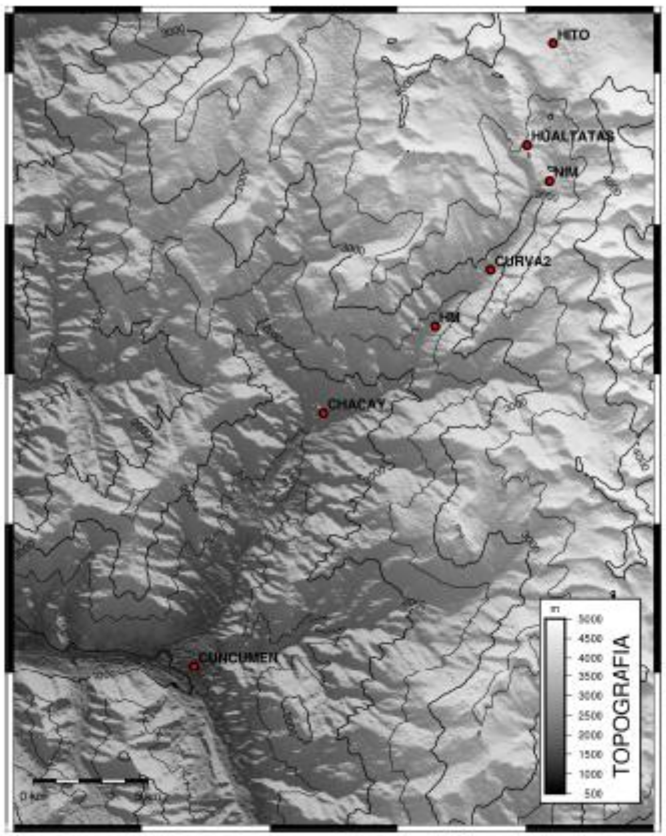

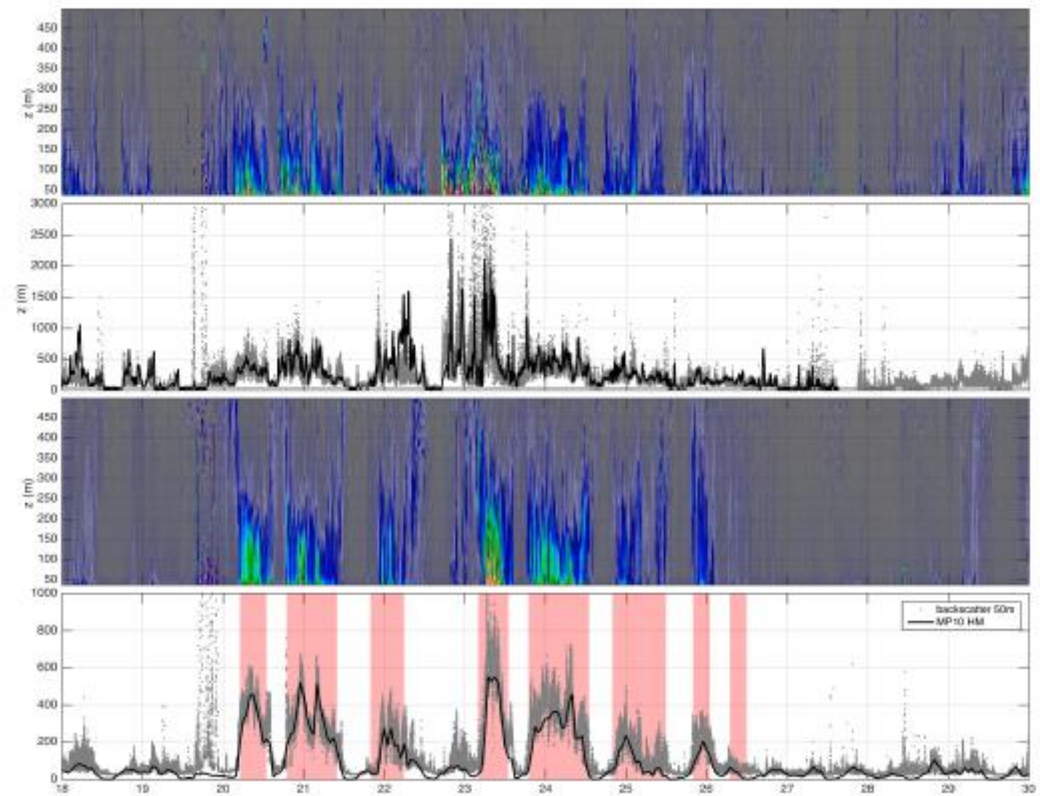

Figura 4.20: a) Backscatter nefo NIM. b) Backscatter nefo en 50 m (puntos grises) y MP10 en NIM (línea negra). c) Backscatter nefo en HM. d) Backscatter nefo en 50m (puntos grises) y MP10 en HM (línea negra). Las bandas color rojo indican los periodos clasificados como Terral.

Journal of Aerosol Science 92 (2016) 16–26

Optical characterization of lower tropospheric aerosols by the Southern East Pacific Lidar station (Concepcion, Chile)

E. Montilla-Rosero [a,b,*], A. Silva [a,b,1], C. Jimenez [a], R. Hernandez [a,b], C. Saavedra [a,b]

Fig. 1. Lidar-CEFOP Observatory facility.

Fig. 2. Geographical location of the city of Concepcion and Lidar station (Google maps).

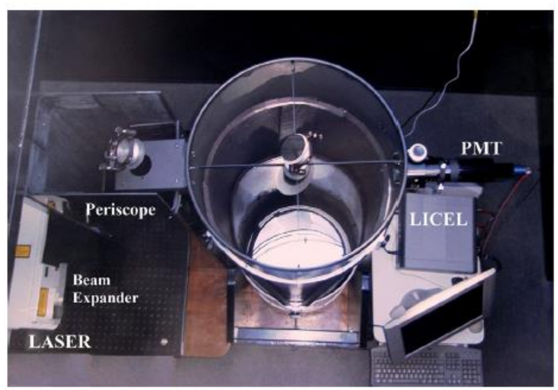

Fig. 3. Set-up of the backscattered Lidar system of CEFOP (Top of view).

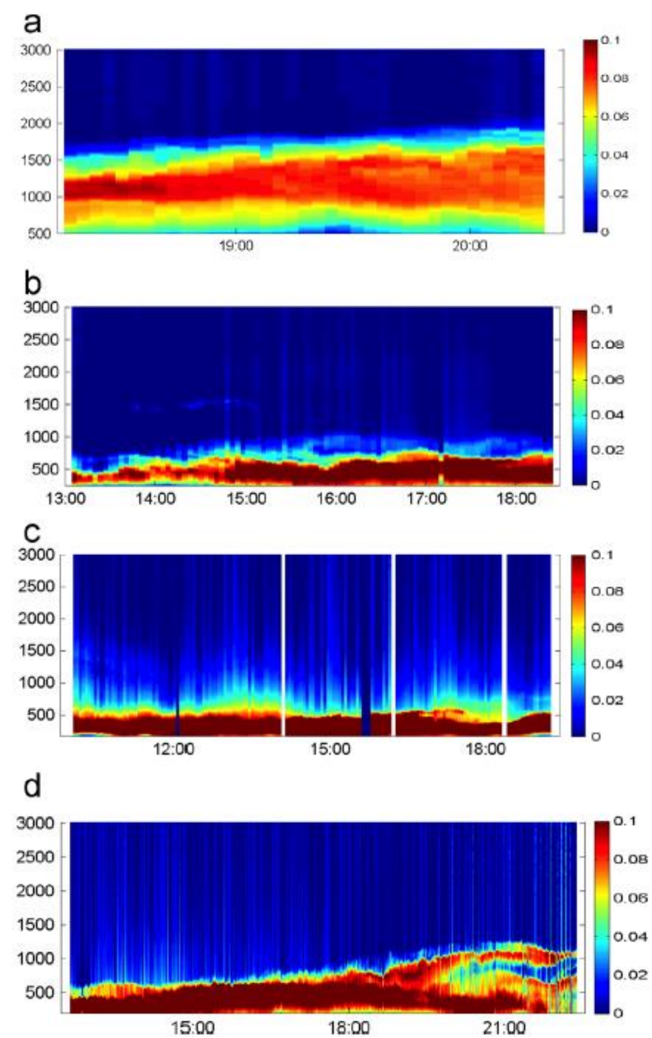

Atmos. Chem. Phys., 20, 8003–8015, 2020
https://doi.org/10.5194/acp-20-8003-2020

Atmospheric Chemistry and Physics
Open Access
EGU

Smoke of extreme Australian bushfires observed in the stratosphere over Punta Arenas, Chile, in January 2020: optical thickness, lidar ratios, and depolarization ratios at 355 and 532 nm

Kevin Ohneiser[1], Albert Ansmann[1], Holger Baars[1], Patric Seifert[1], Boris Barja[2], Cristofer Jimenez[1], Martin Radenz[1], Audrey Teisseire[1], Athina Floutsi[1], Moritz Haarig[1], Andreas Foth[3], Alexandra Chudnovsky[4], Ronny Engelmann[1], Félix Zamorano[2], Johannes Bühl[1], and Ulla Wandinger[1]

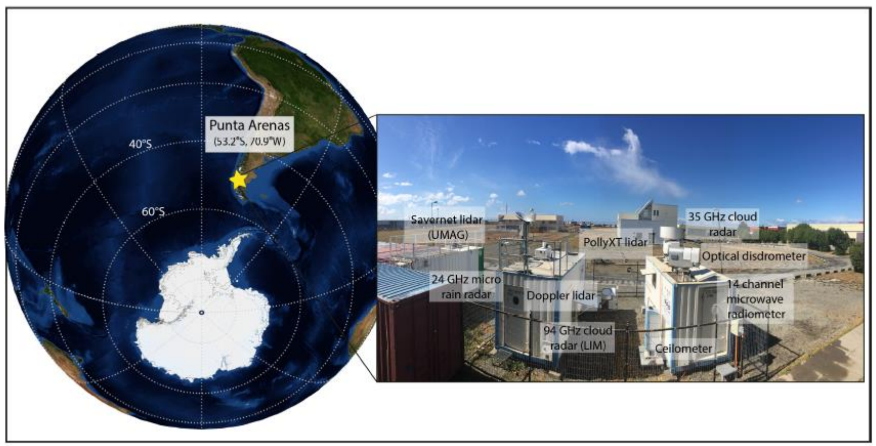

Figure 1. Map of the location of Punta Arenas (indicated by a yellow star) in Chile, South America. The LACROS observational facility, as deployed at UMAG, can be seen on the right side.

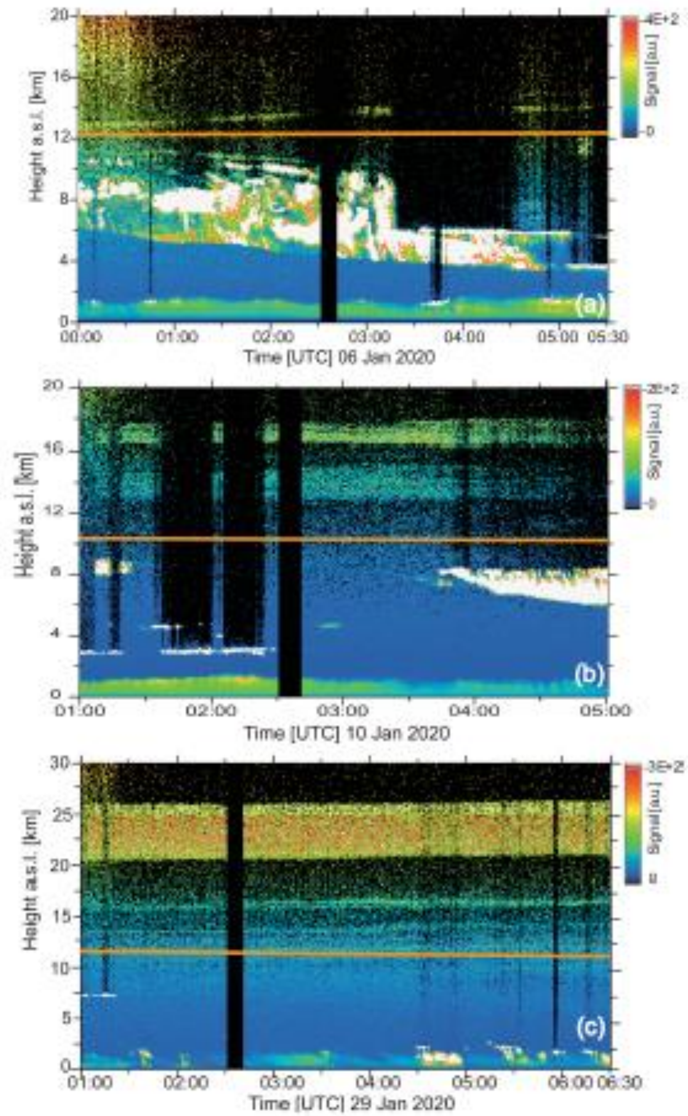

Datos en línea:

Nefo DGF en Santiago:

http://dgf.uchile.cl/~rmunoz/ceilo/fignefoTechoDGFUltimos2Dias.jpg

Nefo DGF en Coyhaique:

http://dgf.uchile.cl/~rmunoz/nefocoihaique/fignefoDGFCoihaiqueUltimos2Dias.jpg

Lidar USACH en Antártica:

https://mplnet.gsfc.nasa.gov/data.cgi?site=King_George_Island